Journal of Computational Physics 229 (2010) 1167–1180

Contents lists available at ScienceDirect

Journal of Computational Physics

journal homepage: www.elsevier.com/locate/jcp

# Compact upwind schemes on adaptive octrees

Scott M. Murman

*NASA Ames Research Center, Moffett Field, CA, USA*

ARTICLE INFO

*Article history:*
Received 18 February 2009
Received in revised form 8 October 2009
Accepted 13 October 2009
Available online 28 October 2009

*Keywords:*
High-order
Finite-volume
Predictor–corrector
Navier–Stokes

ABSTRACT

Compact high-order upwind schemes using reconstruction from cell-averages are derived for application with the compressible three-dimensional Navier–Stokes equations. An adaptive-octree mesh, combined with the Adams–Bashforth–Moulton family of predictor–corrector schemes, provides a conservative high-order time-integration platform supporting localized *h*-refinement and timestep sub-cycling. Numerical examples for smooth flows demonstrate the improvement over explicit upwind schemes and formal accuracy of the schemes, as well as the behavior in wall-bounded regions, and the resolution of a broad wavenumber spectrum.

Published by Elsevier Inc.

## 1. Introduction

Time-dependent numerical simulations which involve disparate length scales, with variations over several orders of magnitude, are a challenge for engineering research and production computing. Examples from the authors research includes foam debris shedding from the space shuttle launch vehicle (SSLV) [1,2], where trajectory predictions of dislodged foam, with a characteristic dimension of roughly one inch, are required over a vehicle hundreds of feet in length. In a jet impinging upon a ground plane in crossflow [3], the jet shear layer contains high-frequency oscillations with Strouhal number roughly $St = \mathcal{O}(10^{-3})$, a von Kármán street forms behind the cylindrical jet with $St = \mathcal{O}(10^{-1})$, and the ground vortex "puffs" with a frequency of $St = \mathcal{O}(10^{1})$. Similarly, predicting the dynamics of atmospheric decelerator systems involves resolution of unsteady wake oscillations over several body diameters, along with small-scale eddies at fractions of a diameter [4]. These examples are further challenged by the associated complex geometry and computational cost of dynamic simulations. Thus, we seek computationally efficient methods of simulating time-dependent motions involving large variations in length scale.

Rather than attempting a global solution, the complex problem is broken into distinct parts: the volume flowfield characterized by temporally-evolving variations over multiple length scales, and a surface near-body region dominated by the complex geometry and numerical stiffness associated with friction and heating. Numerical methods are tailored for the characteristics of each region, and then coupled across the surface-volume interface. Recent examples of these hybrid (finite-volume and finite-difference) schemes include elements of structured, unstructured, and Cartesian approaches [5–7]. The current work focuses solely on the volume off-body region, where reduced numerical stiffness allows the use of efficient and accurate explicit time-integration schemes. Numerical efficiency here encompasses several components: cpu, memory, and bandwidth, both cpu-memory and inter-process bandwidth.

The off-body region requires localized mesh adaptation to effectively resolve the disparate scales, which evolves temporally in response to the (potentially large) unsteady fluid and body motions. An adaptive octree[1] approach (cf. [8,9]), containing structured blocks of fixed size, is used. Adaptive structured blocks facilitate algorithmic and numerical optimizations,

*E-mail address:* Scott.M.Murman@nasa.gov

[1] Sometimes referred to as an unbalanced octree.

0021-9991/$ - see front matter Published by Elsevier Inc.
doi:10.1016/j.jcp.2009.10.019

with low memory overhead. An octree supports hierarchical algorithms, and *a priori* limits the allowable mesh topologies, again enabling tailored optimizations. The adaptive octree is discretized using a finite-volume approach, which facilitates conservative treatment across the octree boundaries, to solve the Navier–Stokes equations. The inviscid operator is treated numerically as a Riemann problem, with the left and right states provided by upwind-biased variable reconstruction schemes.

Higher-order schemes (better than third-order accuracy), coupled with the *h*-refinement of the adaptive octree, potentially offer increases in both accuracy and numerical efficiency. With a multi-block approach, the use of higher-order methods must be balanced against the fixed block size, and the width of the required computational stencil. To take full advantage of the flexibility of an adaptive octree, blocks with a linear dimension of 10–20 degrees of freedom (DoF) are desired. For higher-order schemes which require a seven-point (or greater) stencil width, the overhead in redundant storage to provide boundary communication, i.e. ghost cells, along with the increased communication costs to update the ghost cells in a distributed parallel environment, limit the efficacy of the schemes.

Compact (Padé) schemes [10], which use an implicit reconstruction over a five-point stencil to provide both higher-order accuracy and resolve a broad spectrum of computational wave numbers, provide an attractive alternative to explicit reconstructions. While compact schemes are relatively common for centered finite-difference operators, robust implementations for upwind finite-volume schemes have been slower to develop. Cockburn and Shu [11] extended the upwind flux-vector-splitting method using compact schemes and flux limiters, which was followed contemporaneously in [12–14]. Adams and Shariff developed a hybrid compact finite-difference and ENO scheme for compressible flow [15]. Deng and Maekawa [16], and later Ramboer et al. [17], examined compact reconstruction schemes for the one-dimensional and two-dimensional Euler equations, respectively. Techniques based upon variable extrapolation have also been demonstrated for aeroacoustics [18,19] and electromagnetics [20].

The primary objective of the current work is the development of novel compact upwind schemes using reconstruction from cell-averages, for application on an adaptive-octree finite-volume mesh to compute the three-dimensional compressible Navier–Stokes equations. The focus here is on "smooth" flows that do not contain strong discontinuities, which is the majority of the computational domain for many applications. This is seen as a necessary first step before developing complex nonlinear reconstruction limiters (as an example), or committing to an *h*–*p* framework, to handle general flows. The derived implicit high-order schemes substitute directly for explicit reconstructions in the upwind finite-volume formulation, greatly reducing the numerical dissipation in shock-free regimes, without loss of robustness, or requiring tailored treatments for the boundary closure.

## 2. Compact upwind scheme

To introduce the compact upwind schemes we consider a one-dimensional scalar hyperbolic equation in integral conservation form,

$$\frac{d}{dt}\int_{x_L}^{x_R} u(x,t)dx + f(u(x_R,t)) - f(u(x_L,t)) = 0, \quad \frac{\partial f}{\partial u} \in \Re. \tag{1}$$

For example, $f(u) = \frac{1}{2}u^2$ provides the inviscid Burgers' equation. Introducing the one-dimensional cell size, $h$, and the cell-averaged quantities

$$\bar{u}h = \int_{x_L}^{x_R} u dx = \int_{x-h/2}^{x+h/2} u dx, \tag{2}$$

we have

$$\frac{d}{dt}(\bar{u}h) + f(u(x_R,t)) - f(u(x_L,t)) = 0. \tag{3}$$

The current work uses a polynomial basis to represent the solution,

$$\hat{u}(x) \simeq a_0 + a_1 x + \cdots + a_p x^p = \sum_{k=0}^{p} a_k x^k, \tag{4}$$

so that $\hat{u}(x) = u(x) + \mathcal{O}(h^{p+1})$. It follows then that

$$\hat{f}(\hat{u}) = f(u) + \mathcal{O}\left(h^{p+1}\right), \quad \hat{\bar{u}}(x) = \bar{u}(x) + \mathcal{O}\left(h^{p+1}\right). \tag{5}$$

Introducing a uniform mesh of $N$ cells, indexed with $j \in [0, N-1]$, and simplifying the notation with

$$u \leftarrow \hat{u}, \quad f \leftarrow \hat{f},$$

the semi-discrete approximation of Eq. (3) in cell $j$ is

$$\frac{d}{dt}(\bar{u}_j h) + f_{j+\frac{1}{2}}\left(u\left(x_{j+\frac{1}{2}}, t\right)\right) - f_{j-\frac{1}{2}}\left(u\left(x_{j-\frac{1}{2}}, t\right)\right) = 0. \tag{6}$$

The flux, $f(u)$, is treated as a Riemann problem

$$f_{j+\frac{1}{2}}\left(u_{j+\frac{1}{2}}\right) = f^{RP}_{j+\frac{1}{2}}\left(u^L_{j+\frac{1}{2}}, u^R_{j+\frac{1}{2}}\right). \tag{7}$$

The discrete representation for the left and right states of the Riemann problem at the cell interface, $u^L_{j+\frac{1}{2}}$ and $u^R_{j+\frac{1}{2}}$, are obtained using an upwind reconstruction from the cell-averaged quantities. The formal (asymptotic as $h \to 0$) spatial accuracy of the flux balance (residual) is thus determined by the order of the polynomial basis used to reconstruct the states at each cell interface.

In the schemes considered here, it is sufficient to analyze the reconstruction for $u^L_{j+\frac{1}{2}}$, with $u^R_{j+\frac{1}{2}}$ simply being a reflection. For reference, and to make the notation concrete, explicit upwind reconstructions for basis $p \in [0, 4]$ are presented in Eqs. (8)–(12). The support for the second-and third-order accurate schemes span five computational cells to solve the Riemann problem, with the higher-order schemes using a seven-point stencil. The linear basis uses Fromm's scheme. The explicit schemes for $p \geqslant 3$ are representative of the reconstructions used as a functional basis in WENO schemes [21]

$$p = 0, \quad u^L_{j+\frac{1}{2}} = \bar{u}_j, \tag{8}$$

$$p = 1, \quad u^L_{j+\frac{1}{2}} = \bar{u}_j + \frac{1}{4}(\bar{u}_{j+1} - \bar{u}_{j-1}), \tag{9}$$

$$p = 2, \quad u^L_{j+\frac{1}{2}} = \bar{u}_j + \frac{1}{3}(\bar{u}_{j+1} - \bar{u}_j) + \frac{1}{6}(\bar{u}_j - \bar{u}_{j-1}), \tag{10}$$

$$p = 3, \quad u^L_{j+\frac{1}{2}} = \bar{u}_j + \frac{1}{12}(\bar{u}_{j-2} - 5\bar{u}_{j-1} + \bar{u}_j + 3\bar{u}_{j+1}), \tag{11}$$

$$p = 4, \quad u^L_{j+\frac{1}{2}} = \bar{u}_j + \frac{1}{60}(2\bar{u}_{j-2} - 13\bar{u}_{j-1} - 13\bar{u}_j + 27\bar{u}_{j+1} - 3\bar{u}_{j+2}). \tag{12}$$

To formalize the derivation of the compact upwind schemes, we use a primitive function from the definition of an anti-derivative,

$$U' = \frac{dU(x)}{dx} \equiv u(x), \quad \int_{x_L}^{x_R} u(x)dx = U(x_R) - U(x_L) = \bar{u}h. \tag{13}$$

We thus seek discrete approximations for the derivatives $U'$ at the cell interfaces to reconstruct the states from cell-averaged quantities. Following Lele [10], these are derived from a general Padé approximation to the derivative using a five-point stencil width. Here we use an unbalanced linear combination of derivatives, rather than the centered formulation commonly used in finite-difference approximations. For the $p = 3$ basis we have

$$\beta_3 U'_{j-\frac{1}{2}} + U'_{j+\frac{1}{2}} + \alpha_3 U'_{j+\frac{3}{2}} = a_3\left(\frac{U_{j-\frac{1}{2}} - U_{j-\frac{3}{2}}}{h}\right) + b_3\left(\frac{U_{j+\frac{1}{2}} - U_{j-\frac{1}{2}}}{h}\right) + c_3\left(\frac{U_{j+\frac{3}{2}} - U_{j+\frac{1}{2}}}{h}\right) \tag{14}$$

and similarly for $p = 4$,

$$\beta_4 U'_{j-\frac{1}{2}} + U'_{j+\frac{1}{2}} + \alpha_4 U'_{j+\frac{3}{2}} = a_4\left(\frac{U_{j-\frac{1}{2}} - U_{j-\frac{3}{2}}}{h}\right) + b_4\left(\frac{U_{j+\frac{1}{2}} - U_{j-\frac{1}{2}}}{h}\right) + c_4\left(\frac{U_{j+\frac{3}{2}} - U_{j+\frac{1}{2}}}{h}\right) + d_4\left(\frac{U_{j+\frac{5}{2}} - U_{j+\frac{3}{2}}}{h}\right). \tag{15}$$

The coefficients $\beta_p, a_p, b_p, c_p$, and $d_p$ are determined by matching the Taylor-series coefficients for an expansion about $j + \frac{1}{2}$ of $\mathcal{O}(h^{p+1})$, and leaving $\alpha_p$ as a free parameter. This gives,

$$\beta_3 = 1 - 3\alpha_3, \quad a_3 = \frac{1 - 4\alpha_3}{6}, \quad b_3 = \frac{5 - 11\alpha_3}{3}, \quad c_3 = \frac{1 + 14\alpha_3}{6} \tag{16}$$

and

$$\beta_4 = \frac{2}{3} - \alpha_4, \quad a_4 = \frac{1 - 2\alpha_4}{12}, \quad b_4 = \frac{47 - 54\alpha_4}{36}, \quad c_4 = \frac{11 + 54\alpha_4}{36}, \quad d_4 = \frac{-1 + 6\alpha_4}{36}. \tag{17}$$

At this point it is straightforward to perform a spectral analysis of Eqs. (14) and (15) to determine the damping and dispersion properties of the schemes, and then use a heuristic to determine the free parameter $\alpha_p$. In practice this approach provides only cursory value, as the applications considered here require reconstructions on a finite, rather than periodic, domain. With a finite domain, the treatment of the lower and upper boundaries greatly influences the properties of the implicit reconstruction schemes. Common boundary treatments for compact schemes (primarily finite-difference) include reducing the order of the basis approaching the boundary (often *via* filtering), switching to downwind-biased reconstructions, or combinations thereof (cf. [22,23]).

The approach taken here is to treat the boundary and interior formulations holistically, and determine the free parameter $\alpha_p$ and the boundary formulation concurrently to provide a reconstruction that is both accurate and stable for nonlinear systems on a finite domain. The lower boundary ($j = -\frac{1}{2}$ denoted by subscript $lb$) uses an implicit downwind-biased stencil,

$$U'_{-\frac{1}{2}} + \alpha_{lb} U'_{\frac{1}{2}} = a_{lb}\left(\frac{U_{-\frac{1}{2}} - U_{-\frac{3}{2}}}{h}\right) + b_{lb}\left(\frac{U_{\frac{1}{2}} - U_{-\frac{1}{2}}}{h}\right) + c_{lb}\left(\frac{U_{\frac{3}{2}} - U_{\frac{1}{2}}}{h}\right) + d_{lb}\left(\frac{U_{\frac{5}{2}} - U_{\frac{3}{2}}}{h}\right) + e_{lb}\left(\frac{U_{\frac{7}{2}} - U_{\frac{5}{2}}}{h}\right). \tag{18}$$

The upper boundary (subscript $ub$) is a mirror image. The coefficients $a_{lb}, b_{lb}, c_{lb}, d_{lb}$, and $e_{lb}$ are again determined by matching the Taylor-series coefficients for an expansion about $j = -\frac{1}{2}$ based on $p = 4$, leaving $\alpha_{lb}$ as a free parameter. Both the $p = 3$ and $p = 4$ interior schemes use the same boundary formulation. This gives

$$a_{lb} = \frac{2\alpha_{lb} - 3}{60}, \quad b_{lb} = \frac{27 - 13\alpha_{lb}}{60}, \quad c_{lb} = \frac{47\alpha_{lb} + 47}{60}, \quad d_{lb} = \frac{27\alpha_{lb} - 13}{60}, \quad e_{lb} = \frac{2 - 3\alpha_{lb}}{60}. \tag{19}$$

Further, we prescribe $\beta_{ub} = \frac{1}{\alpha_{lb}}$ based upon symmetry considerations.

The linear stability of the coupled interior and boundary scheme is analyzed for the scalar advection equation, $f(u) = au, a > 0$, using a modal approach. Writing the compact reconstruction as a matrix operator[2] gives

$$u^L_{j+\frac{1}{2}} = \hat{\boldsymbol{L}}(\bar{u}_j) = \boldsymbol{V}^{-1}\boldsymbol{W}\bar{u}_j \tag{20}$$

and for $p = 3$

$$\boldsymbol{V} = \begin{bmatrix} 1 & \alpha_{lb} & 0 & \dots \\ \beta_3 & 1 & \alpha_3 & \dots \\ 0 & \ddots & \ddots & \dots \\ \dots & & & \\ \dots & 0 & \beta_{ub} & 1 \end{bmatrix}, \quad \boldsymbol{W} = \begin{bmatrix} a_{lb} & b_{lb} & c_{lb} & d_{lb} & e_{lb} & 0 & \dots \\ 0 & a_3 & b_3 & c_3 & 0 & 0 & \dots \\ 0 & 0 & \ddots & \ddots & \ddots & 0 & \dots \\ \dots & & & & & & \\ \dots & 0 & e_{ub} & d_{ub} & c_{ub} & b_{ub} & a_{ub} \end{bmatrix}.$$

From $\hat{\boldsymbol{L}}$ we construct the flux difference, and write the semi-discrete equation along the one-dimensional line as a linear mapping operator $\boldsymbol{L}$,

$$\frac{d\bar{u}_j}{dt} = \boldsymbol{L}(\bar{u}_j). \tag{21}$$

For an explicit scheme $\boldsymbol{L}$ is a banded matrix, while for the implicit reconstruction the matrix is full. The solution to Eq. (21) is given by

$$\bar{u}_j(t) = \sum_j \boldsymbol{v}_j e^{\lambda_j t} + \bar{u}_p(t), \tag{22}$$

where $\lambda_j$ are the eigenvalues of $\boldsymbol{L}$, and $\bar{u}_p$ is a particular solution which does not effect the linear stability. Thus, the necessary condition for linear stability of the coupled interior and boundary scheme is that the eigenvalues of $\boldsymbol{L}$ all inhabit the left half of the complex plane, i.e. $\mathrm{Re}(\lambda_j) \leqslant 0\ \forall j$.

The linear stability criteria provide necessary conditions for the compact upwind schemes, however in practice linear stability alone is not sufficient to ensure satisfactory performance for nonlinear problems on irregular mesh topologies in multiple dimensions. Additional criteria pertinent to nonlinear systems containing multiple waves of opposing sign are necessary. In the current approach, the free interior and boundary parameters for the compact upwind schemes are chosen to satisfy the linear stability criteria and also completely annihilate the high-frequency (Nyquist) odd–even spectral modes between the left and right states at the cell interface, as occurs naturally with the explicit schemes Eqs. (8)–(12). This is formulated as a constrained optimization problem,

**Given**: $u_j(x) = u_\circ \sin\left(\frac{\pi x_j}{h} + \phi\right)$
**Find**: $\alpha_p$ and $\alpha_{lb}$ such that

$$\hat{\boldsymbol{L}}(\bar{u}_j) = u^L_{j+\frac{1}{2}} = \hat{u}_\circ \sin\left(\frac{\pi x_j}{h}\right)$$
$$u^R_{j+\frac{1}{2}} = \hat{u}_\circ \sin\left(\frac{\pi x_j}{h} + \pi\right)$$

where $\hat{u}_\circ \leqslant u_\circ$ and $\mathrm{Re}(\lambda_j) \leqslant 0\ \forall j$.

and solved using a genetic algorithm. A set of solutions for this problem provides the parameters

$$\alpha_3 = \frac{1}{5}, \quad \alpha_4 = \frac{1}{4}, \quad \alpha_{lb} = 9, \tag{23}$$

which completes the derivation of the compact upwind schemes for $p \in [3, 4]$.

[2] The mixed notation treats the discrete representation along a one-dimensional line as a vector.

Eigenvalues from the modal analysis of the $p = 3$ compact scheme are presented in Fig. 1 for a sampling of the interior and boundary parameters. From the standpoint of linear stability there appears little to distinguish the final coefficients from reasonable alternatives. The explicit and final forms of the compact schemes are presented in the modal analysis context in Fig. 2.

The compact high-order reconstructions are tridiagonal equations which are solved along a one-dimensional line to determine the cell interface states. Two inversions are required, one each for $u^L_{j+\frac{1}{2}}$ and $u^R_{j+\frac{1}{2}}$, in order to solve the Riemann problem. Compact representations of central-difference gradients for the flux are obtained in a single tridiagonal inversion, however these schemes also require implicit filtering or artificial dissipation in order to maintain stability, hence the computational costs roughly balance in one dimension. The multi-dimensional implementation of the finite-volume scheme is covered in more detail in Section 3. Relative to Fromm's scheme, the compact schemes require roughly 10–20% greater computational cost (depending upon hardware, compiler, etc.).

The formal accuracy of the compact schemes is demonstrated by reconstructing a sinusoidal function,

$$u_{ex}(x) = \sum_{n=1}^{10} A_n \sin\left(2n\pi\frac{x}{L} + \phi_n\right), \tag{24}$$

where the amplitude and phase shift for each harmonic are determined from a random draw. While this function is periodic over $x \in [0, L]$, the reconstruction is performed on a finite domain with the appropriate number of ghost cells transferred from the circular boundary. Fig. 3 presents the sinusoidal function, and the convergence obtained using isotropic refinement of the one-dimensional mesh for each of the explicit and implicit reconstruction schemes presented above. The slope of the convergence between the finest two resolutions tested, $N = 2^8$ and $N = 2^9$, is noted near the terminus of each line. Each scheme achieves the predicted formal accuracy, $\mathcal{O}(h^{p+1})$, as $h \to 0$. The compact schemes reach this asymptotic state at coarser resolution than the explicit schemes, and have lower error than the explicit schemes of similar basis, independent of the resolution.

## 3. Adaptive-octree sub-cycling

Extending the one-dimensional scalar hyperbolic equation of Section 2 to the three-dimensional Euler equations we have

$$\frac{d}{dt}\int \boldsymbol{Q} dV + \oint \boldsymbol{f}\cdot\boldsymbol{n} dS, \quad S = \partial V, \tag{25}$$

where $\boldsymbol{Q}$ are the conserved quantities and $\boldsymbol{f}$ is the inviscid flux,

$$\boldsymbol{Q} = \begin{pmatrix} \rho \\ \rho\boldsymbol{u} \\ \rho e \end{pmatrix}, \quad \boldsymbol{f}\cdot\boldsymbol{n} = \begin{Bmatrix} \rho u_n \\ \rho u_n \boldsymbol{u} + p\boldsymbol{n} \\ \rho u_n e + p\boldsymbol{u}\cdot\boldsymbol{n} \end{Bmatrix}, \quad u_n = \boldsymbol{u}\cdot\boldsymbol{n}$$

This system of equations is solved numerically using a finite-volume approach on an adaptive-octree mesh (cf. Fig. 4). The adaptive octree uses isotropic Cartesian blocks of fixed dimensions, also referred to as nodes, which are constrained during adaptation so the maximum difference in both resolution and depth is one between distance-1 neighbors in the tree. This provides a flexible and efficient infrastructure for problems involving large variations in the characteristic length scale, for example using localized $h$-refinement to resolve finer structures. With the nodal approach, the numerical scheme in each

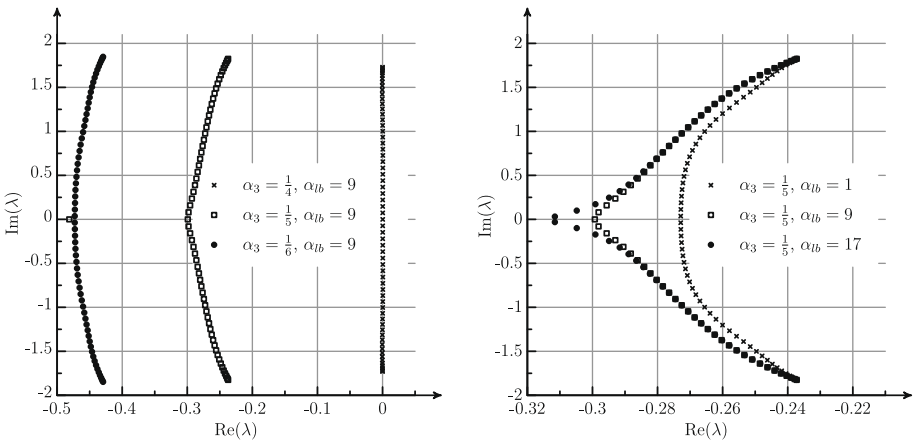


**Fig. 1.** Eigenvalues of the compact linear mapping operator, Eq. (21), with $N = 64$.

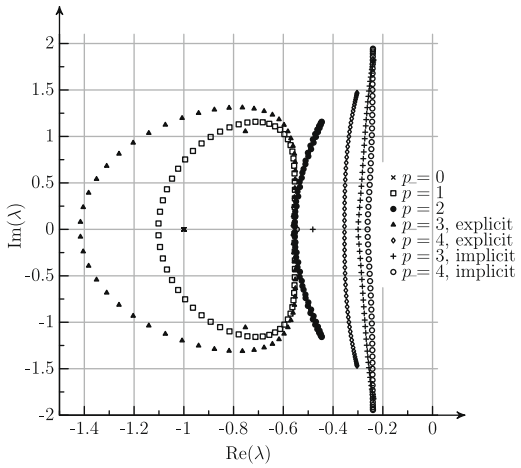


**Fig. 2.** Eigenvalues of the upwind linear mapping operators with $N = 64$.

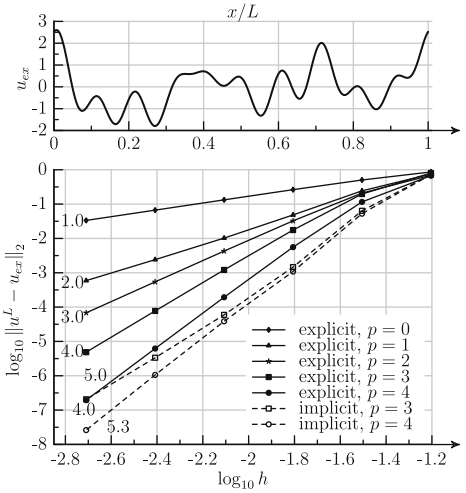


**Fig. 3.** Convergence of the reconstruction for a sinusoidal function with random amplitudes and phase shift over the first 10 harmonics. The slope of the convergence between the finest two resolutions tested is noted near the terminus of each line. The explicit schemes are given by Eqs. (8)–(12). The implicit schemes are summarized in Eqs. (14) and (15).

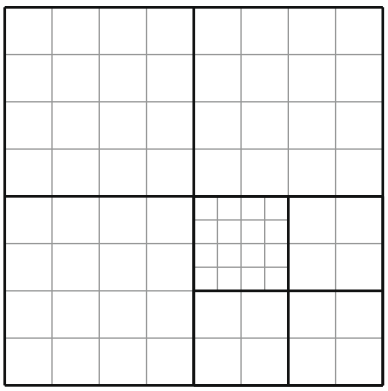

**Fig. 4.** Cutting plane through a sample adaptive-octree mesh with three levels of refinement and node dimension $N = 4$. Each node in the tree is outlined with thicker boundary lines.

block can be tailored to the relevant flow physics, e.g. non-oscillatory schemes in regions containing strong discontinuities. In this work we only consider regions of "smooth" flow, where the upwind schemes outlined in the previous section are applied unaltered.

Each node maintains ghost cells to support the width of the stencil for the spatial reconstruction, i.e. two layers of ghost cells at each nodal boundary for the five-point compact schemes. This ghost-cell data is either supplied by the neighboring nodes, or domain boundary conditions. There are three types of ghost-cell data transfer between nodes: direct injection when the resolutions across the nodal boundary are identical, averaging when the donor node is finer than the receiver, and interpolation when the donor is coarser. The first two cases are straightforward, while interpolation requires some explanation. When discussing two discrete resolutions, $H$ refers to the coarser resolution, and $h$ the finer.

Exchanging ghost-cell data from a coarse donor to a finer receiver node uses the polynomial basis of the donor node, along with conservation, to determine appropriate interpolation coefficients. For example, using a linear basis we have for the interpolation function, $\boldsymbol{\phi}(x) = \boldsymbol{a}_0 + \boldsymbol{a}_1 x$, with the coefficients $\boldsymbol{a}_0$ and $\boldsymbol{a}_1$ determined by requiring

$$\int_{-\frac{H}{2}}^{\frac{H}{2}} \boldsymbol{\phi}(x)dx = \bar{\boldsymbol{Q}}_0^H H, \quad \int_{\frac{H}{2}}^{\frac{3H}{2}} \boldsymbol{\phi}(x)dx = \bar{\boldsymbol{Q}}_1^H H, \tag{26}$$

with $\bar{\boldsymbol{Q}}_j^H$ being the cell-averaged state on the coarse node. The ghost-cell data for the finer node then is given by

$$\begin{aligned} \bar{\boldsymbol{Q}}_{G0}^h h &= \int_{-\frac{h}{2}}^{\frac{h}{2}} \boldsymbol{\phi}(x)dx = \int_{-\frac{H}{2}}^{0} \boldsymbol{\phi}(x)dx, \\ \bar{\boldsymbol{Q}}_{G1}^h h &= \int_{\frac{h}{2}}^{\frac{3h}{2}} \boldsymbol{\phi}(x)dx = \int_{0}^{\frac{H}{2}} \boldsymbol{\phi}(x)dx. \end{aligned} \tag{27}$$

Higher-order polynomials are handled similarly. In multiple dimensions the interpolations are built using tensor products of the one-dimensional interpolants.

This interpolation procedure results in aliasing of the solution, whereby spectral modes which cannot be represented on the coarser resolution are created on the finer resolution through the interpolation. This effect is remedied by filtering the interpolated ghost-cell data after it is generated on the finer resolution. The ideal filter is an ideal low-band-pass filter (sinc filter) centered on $\kappa h = \frac{\pi}{2}$, where $\kappa h$ is the discrete spectral wavenumber of the fine mesh spatial resolution. Frequencies higher than $\kappa h = \frac{\pi}{2}$ cannot be supported on the coarser mesh, and hence are spurious when transferred to the finer resolution. The current work uses an explicit sixth-order filter,

$$\bar{u}_j' = \frac{44}{64}\bar{u}_j + \frac{15}{64}\left(\bar{u}_{j+1} + \bar{u}_{j-1}\right) - \frac{6}{64}\left(\bar{u}_{j+2} + \bar{u}_{j-2}\right) + \frac{1}{64}\left(\bar{u}_{j+3} + \bar{u}_{j-3}\right), \quad \forall j \in [1, N-2]. \tag{28}$$

This filtering procedure does not affect global conservation, as conservation is ensured by performing a correction to the numerical flux between $h$-refinement nodes, as described below.

To integrate Eq. (25) forward in time we use the method of lines to solve the semi-discrete equations as a system of ordinary differential equations (ODE). Writing the semi-discrete version of Eq. (25) as an ODE, and simplifying for an isotropic cell, we have

$$\frac{d\bar{\boldsymbol{Q}}_j}{dt} = \boldsymbol{R}(\bar{\boldsymbol{Q}}_j), \quad \boldsymbol{R}(\bar{\boldsymbol{Q}}_j) = -\frac{1}{h}\sum_{\partial V}\left[\sum_{m=1}^{q^2} w_m \boldsymbol{f}^{RP}\left(\boldsymbol{Q}_m^L, \boldsymbol{Q}_m^R\right)\cdot \boldsymbol{n}\right], \tag{29}$$

where each cell interface uses an $q$-point Gaussian quadrature of the flux, with weight $w_m$, which is exact for polynomials with basis $p = 2q - 1$. The inviscid flux is again treated as a Riemann problem, with $\boldsymbol{Q}_m^L$ and $\boldsymbol{Q}_m^R$ being the reconstructed left and right states at the Gaussian quadrature points. Intermediate points are first interpolated in the transverse directions, from which the cell interface states at the quadrature points are reconstructed using the one-dimensional formulas of Section 2. As the flows here are shock-free, the transverse constructions use straightforward polynomial interpolation of $\mathcal{O}(h^{2q-1})$.

A simplifying approximation uses a single-point Gaussian quadrature on the isotropic mesh, with the quadrature point at the face centroid and unit weighting. The residual in Eq. (29) thus simplifies to

$$\boldsymbol{R}(\bar{\boldsymbol{Q}}_j) = -\frac{1}{h}\sum_{\partial V}\boldsymbol{f}^{RP}\left(\boldsymbol{Q}^L, \boldsymbol{Q}^R\right)\cdot \boldsymbol{n} \tag{30}$$

and the computational cost likewise is reduced as a single Riemann problem is required at each interface, and the transverse reconstruction is avoided. The numerical examples in this work produce nearly identical results with the higher-order schemes using the single-point or multiple-point quadrature formulas.

Integrating Eq. (29) on the adaptive-octree mesh, the scheme adapts to the local length scale by adjusting the timestep in each node. A constant ratio of discrete timestep to spatial resolution is maintained as the octree is traversed, so that the time integration is "sub-cycled" on the finer resolution nodes, as with the Adaptive Mesh Refinement (AMR) approach [24]. Thus,

large variations in time scale, either correlated with the length scale or independent, are efficiently captured using local temporal refinement.

The adaptive-octree approach uses the Adams–Bashforth–Moulton (ABM) predictor–corrector schemes of the same polynomial basis as the spatial reconstruction. The ABM schemes are given by

$$\bar{\mathbf{Q}}_j^{\prime} = \bar{\mathbf{Q}}_j^n + \frac{Cn}{S}\left[\sum_{i=0}^{p} \beta_i^{\prime} \mathbf{R}^{n-i}(\bar{\mathbf{Q}}_j)\right], \tag{31}$$

$$\bar{\mathbf{Q}}_j^{n+1} = \bar{\mathbf{Q}}_j^n + \frac{Cn}{S}\left[\beta_0 \mathbf{R}\left(\bar{\mathbf{Q}}_j^{\prime}\right) + \sum_{i=0}^{p-1} \beta_i \mathbf{R}^{n-i}(\bar{\mathbf{Q}}_j)\right], \tag{32}$$

with the discrete time level given by $n\Delta t$, and using a constant Courant number, $Cn = \frac{S\Delta t}{h}$ in each octree node. The wave speed, $S$, is likewise constant across the computational domain. The coefficients for the ABM schemes, and estimates of the local truncation error, are easily derived (cf. [25]). The ABM schemes use two residual evaluations independent of the order of accuracy. In many applications the temporal truncation error is orders of magnitude lower than the spatial truncation error. This is monitored using the predictor–corrector schemes, and estimates of spatial truncation error available from evaluating the residual with increasing order. When possible, ABM schemes of lower formal accuracy than the spatial resolution are used to provide greater efficiency (due to the greater stability bound) and improved damping properties. Higher-order Runge–Kutta integration methods have an enhanced stability bound (per residual evaluation) compared to the ABM schemes, however the use of high-order R–K schemes causes difficulties when implementing sub-cycling (described below) on the octree mesh.

A one-dimensional $h$-refinement nodal boundary is presented in the $x - t$ plane in Fig. 5. The predictor–corrector sub-cycling process is described. First, the predictor step is computed on the coarse mesh to obtain an estimate of the solution corresponding to time level $t^{n+2}$ on the finer mesh. Using a polynomial basis consistent with the temporal accuracy of the integration scheme, ghost cell data for the finer mesh at time levels $t^{n+1}$ and $t^{n+2}$ is interpolated from the coarse mesh. The finer mesh is then advanced for two predictor–corrector cycles. This provides ghost-cell data for the final corrector step on the coarse mesh, and the solution is advanced using this bootstrapping technique. To accommodate multiple levels of mesh adaptation, the sub-cycling time advance is generalized with a recursive algorithm. This approach requires two ghost cell updates to advance one step on the coarse resolution, one each for the predictor and corrector. Reducing the boundary communication using compact schemes improves the efficiency of the time advance.

The flux on the boundary is accumulated during the cycle, and after the coarse grid time integration, the coarse grid state is corrected by the flux difference between the fine and coarse mesh over $[t^n, t^{n+2}]$ to maintain global conservation, as is done with the AMR approach. In addition, a conservation correction is performed at each $p$-refinement boundary, and at the coterminous nodes for the compact schemes, as the implicit reconstruction depends upon an entire line of data.

The octree timestep sub-cycling requires storage of sufficient time levels to interpolate the polynomial basis in time, as well as space. With the structured adaptive-octree implementation this storage cost is not restrictive. These stored time levels have been used to formulate general linear multistep methods (LMM) with improved damping and stability properties over the ABM schemes. These general LMM schemes integrate over multiple time levels however, which complicates the accounting required for the conservation correction to balance the flux between nodes.

Adaptation involves both refinement and coarsening of the octree mesh. Refinement uses the same interpolation procedures described above for the transfer of ghost-cell data. Refinement also proceeds in time, and the flow state and residual are interpolated in time using standard stencils for the appropriate polynomial basis representing the time advance. Coarsening also follows the averaging procedures for the ghost-cell data, and any unavailable data required at previous time levels is obtained using extrapolation.

## 4. Isentropic vortex convection

Following Yee et al. [26], we demonstrate the properties of the numerical scheme described in Sections 2 and 3 for a planar convecting vortex. The velocity field is a superposition of a uniform flow ($\boldsymbol{u}_\infty$) and an isentropic perturbation due to a rotational line vortex ($\delta \boldsymbol{u}_\psi$), so that

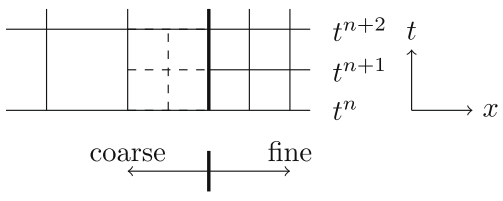


**Fig. 5.** One-dimensional $h$-refinement nodal boundary interface. The ghost cells for the fine grid are outlined with dashed lines.

$$\boldsymbol{u} = \boldsymbol{u}_\infty + \delta\boldsymbol{u}_\psi = \boldsymbol{u}_\infty + \boldsymbol{r} \times \boldsymbol{\psi}. \tag{33}$$

If $\boldsymbol{u}_\infty$ and $\boldsymbol{\psi}$ are perpendicular and the flow is inviscid, then the vortex perturbation behaves as a passive scalar and convects with the uniform flow velocity. A radial distribution is constructed so that

$$\boldsymbol{\psi} = \psi_{max} e^{(1-r^2)/2} \boldsymbol{e}_z, \tag{34}$$

where

$$r^2 = |\boldsymbol{r}| = |(\boldsymbol{x} - \boldsymbol{x}_o)/b| \tag{35}$$

is the scaled distance from the center of the vortex $\boldsymbol{x}_o$. The maximum velocity perturbation is thus located at $|\boldsymbol{x}| = b^2$.

Since Eq. (33) is stationary in a reference frame moving with the uniform flow velocity, the isentropic chain is used to determine the thermodynamic quantities as a function of radial distance from the vortex center,

$$\frac{T}{T_\infty} = \left(\frac{p}{p_\infty}\right)^{(\gamma-1)/\gamma} = \left(\frac{\rho}{\rho_\infty}\right)^{\gamma-1} = 1 - \frac{\gamma-1}{2}\frac{\psi_{max}^2}{a_\infty^2} e^{(1-r^2)}. \tag{36}$$

Here we use a domain of unit width and length, and a vortex radius of $b = 0.05$. The convective velocity is oriented 45° to the coordinate axes and the magnitude is 0.5. The problem assumes an infinite array of identical planar vortices convecting through the computational domain, hence periodic boundary conditions are enforced, i.e. the computation uses algorithms for a finite domain and the ghost cell data is transferred from the circular boundary. Note that the equations for the vortex-induced variations are for a single isolated vortex, hence do not account for the superposition between neighboring vortices, limiting the computational resolution to cases where these effects are negligible relative to the error in the simulation itself. The simulation is run for a total time corresponding to the vortex convecting $100b$ units, which is roughly the length of 3-1/2 domain diagonals. The ABM schemes are not self-starting, so the exact solution is used to initialize the flow state and residual prior to the start of the simulation. The simulations use $Cn = 0.25, S = |\boldsymbol{u}_\infty| + c_\infty = 1.5$, and the AUSM$^+$ flux-vector-splitting scheme [27] throughout. The two-dimensional flow is simulated on a three-dimensional octree mesh by enforcing $\frac{\partial}{\partial z} \equiv 0$ and computing an array of identical solutions in $x - y$.

Simulations with increasing refinement uniformly in space and time are performed by isotropically sub-dividing the octree mesh to increasing depth using a fixed node dimension, $N = 16$. For the explicit spatial reconstruction schemes this is equivalent to increasing the resolution within a mesh containing a single node, however for the implicit schemes this is not the case, as the reconstruction differs striding a block interface. The spatial reconstruction schemes in Section 2 are used in conjunction with the ABM time-integration scheme of the same polynomial basis. The computed solution error in Fig. 6 follows the same trends as the one-dimensional reconstruction, Fig. 3. The explicit schemes of increasing polynomial basis show a reduction in solution error for the same resolution, and are approaching the asymptotic formal accuracy. The implicit schemes show a lower error than the comparable explicit schemes, and approach the asymptotic formal accuracy at coarser resolution. The convergence of the residual with increasing refinement (not shown), follows similar trends as the cell-averaged quantities.

The adaptive-octree mesh outlined in Section 3 allows local refinement and coarsening to improve the efficiency of the simulation beyond isotropic refinement. This adaptation then evolves as the simulation advances in time. There are a variety of methods for specifying adaptation criteria, e.g. feature-based, output-based (adjoint), local truncation error, etc. The focus here is not on the specifics of solution adaptation for time-varying flows, a subject which requires a thorough treatment on

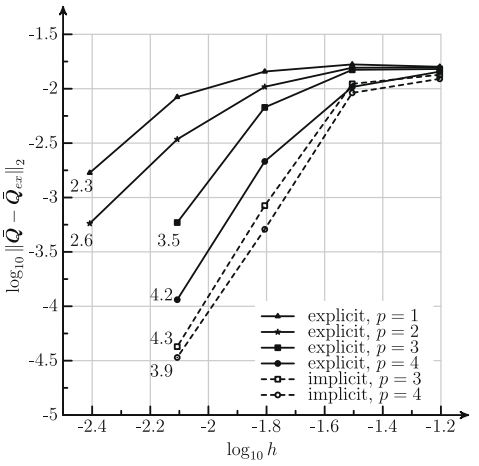


**Fig. 6.** Convergence of the isentropic vortex convection using isotropic refinement. The slope of the convergence between the finest two resolutions tested is noted near the terminus of each line. The explicit schemes are given by Eqs. (9)–(12). The implicit schemes are summarized in Eqs. (14) and (15).

its own. The intent is to demonstrate the flexibility and efficiency of the adaptive-octree infrastructure; one which facilitates the use of many adaptation criteria. Hence, adaptation is prescribed to follow the theoretical position and extent of the convecting vortex. The explicit $p = 3$ and 4 schemes with seven-point stencil width are omitted from this test for brevity.

Fig. 7 repeats the isotropic refinement data, and contains the solution error on a series of simulations increasing the maximum allowable resolution during the adaptive refinement. The error in the $L_2$-norm is then plotted against the average resolution over the simulation for the adaptive results. Each scheme shows an improvement in efficiency (comparable error levels using fewer degrees of freedom) for the adaptive simulations. There is little to distinguish the computed results between the compact upwind schemes on the adaptive meshes. Snapshots of the octree mesh and computed density contours for the finest resolution adaptive mesh computed with the $p = 3$ compact scheme are presented in Fig. 8. Within each octree node the solution state is averaged at the cell vertices to support the contouring, and remains disjoint between octree nodes. The low diffusion and dispersion of the vortex is apparent, and the contours do not exhibit high-frequency oscillations.

## 5. Laminar flat plate

The non-dimensional equations for compressible viscous flow in integral conservation form are written as

$$\frac{d}{dt}\int \mathbf{Q}dV + \oint (\boldsymbol{f} - \boldsymbol{g})\cdot \boldsymbol{n}dS, \quad S = \partial V, \tag{37}$$

where $\boldsymbol{g}$ is the viscous flux

$$\boldsymbol{g} = Re_{\text{ref}}^{-1}\begin{pmatrix} 0 \\ \boldsymbol{\tau} \\ \boldsymbol{u}\cdot\boldsymbol{\tau} + Pr_{\text{ref}}^{-1}Ec_{\text{ref}}^{-1}\kappa\nabla T \end{pmatrix}, \quad \boldsymbol{\tau} = \mu\left(\nabla\boldsymbol{u} + \nabla\boldsymbol{u}^T\right) + \lambda\nabla\cdot\boldsymbol{u}\boldsymbol{I}. \tag{38}$$

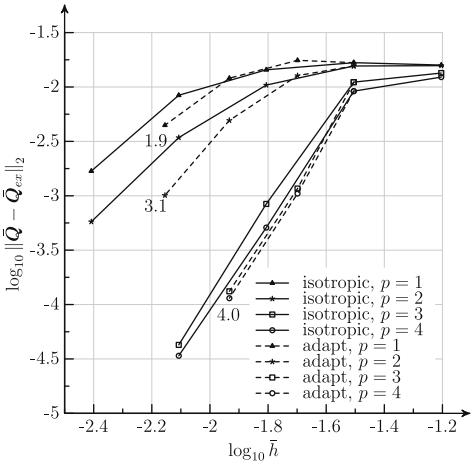


**Fig. 7.** Convergence of the isentropic vortex convection using adaptive refinement. The slope of the convergence between the finest two resolutions tested is noted near the terminus of each line. The explicit schemes are given by Eqs. (9) and (10). The implicit schemes are summarized in Eqs. (14) and (15).

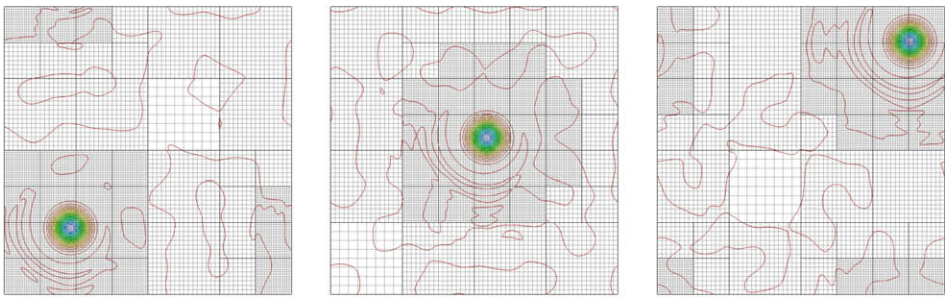


**Fig. 8.** Normalized density contours ($\rho \in [0.9\rho_\infty, \rho_\infty]$) for the finest adaptive mesh computed using the $p = 3$ compact upwind scheme. Within each octree node the solution state is averaged at the cell vertices to support the contouring and remains disjoint between octree nodes. The nodal boundaries are outlined for clarity.

The non-dimensional groups are the reference flow Reynolds number, Prandtl number for the fluid, and the Eckert number, respectively

$$Re_{\text{ref}} = \frac{\rho_{\text{ref}} u_{\text{ref}} L_{\text{ref}}}{\mu_{\text{ref}}}, \quad Pr_{\text{ref}} = \frac{\mu_{\text{ref}} c_{p_{\text{ref}}}}{\kappa_{\text{ref}}}, \quad Ec_{\text{ref}} = \frac{u_{\text{ref}}^2}{c_{p_{\text{ref}}} T_{\text{ref}}}.$$

The inviscid flux in Eq. (37) is treated as a Riemann problem as discussed in Sections 2–4. The diffusive terms are discretized using (non-compact) centered five-point differences ($p = 3$) for the gradients parallel to the face normal, and centered three-point differences ($p = 1$) for the transverse gradients.

In addition to the time-dependent formulation outlined in Section 3, an efficient smoother is required to remove start-up transients and when computing time-invariant problems. The time-invariant semi-discrete ODE for Eq. (37) is given by,

$$\frac{d\bar{\mathbf{Q}}_j}{dt_j} = \boldsymbol{R}(\bar{\mathbf{Q}}_j), \tag{39}$$

with $t_j$ a local timescale in each cell, and $\boldsymbol{R}$ the summation of the inviscid and viscous balance. This is iterated using an explicit multistage scheme

$$\begin{aligned} \bar{\mathbf{Q}}_j^0 &= \bar{\mathbf{Q}}_j^n, \\ \bar{\mathbf{Q}}_j^k &= \bar{\mathbf{Q}}_j^n + \gamma_k \Delta t_j \boldsymbol{R}\left(\bar{\mathbf{Q}}_j^{k-1}\right), \quad k \in [0, m], \\ \bar{\mathbf{Q}}_j^{n+1} &= \mathbf{Q}_j^m, \end{aligned} \tag{40}$$

with $m = 5$, and $\gamma_k = 2^{k-m}$. To efficiently remove long wavelengths from the residual error, especially for the compact high-order schemes, the explicit multistage scheme is used as the smoother in a $p$-multigrid framework (cf. [28]). A V-cycle is used with a full-approximation-storage scheme. The coarser polynomial basis to each level in the multigrid hierarchy is specified as

$$p^C = p^c \bmod 2, \quad \forall p^c > 0, \tag{41}$$

where $p^C$ and $p^c$ are the coarser and finer polynomial bases respectively.

Simulations of the laminar flow over a flat plate exercise the viscous flux formulation and the iterative scheme. The streamwise pressure gradient is zero, and comparisons against the theoretical Blasius velocity profile are presented. The solid wall is impermeable, adiabatic, and uses the boundary-layer approximation $\frac{\partial p}{\partial y} = 0$. An inviscid wall section is utilized upstream of the plate leading edge. A parabolic velocity profile is specified at the inflow plane to reduce the (numerical) leading-edge effects, along with a Riemann-based boundary condition. The freestream Mach number is $M_\infty = 0.2$, and the Reynolds number based upon the length of the plate is $Re_L = 10^4$. Roe's approximate Riemann solver [29] is used throughout.

Fig. 9 presents the residual convergence of the $p$-multigrid iterative scheme for the $p = 3$ compact spatial operator on a series of meshes with increasing resolution. The polynomial bases are not hierarchical, and hence the asymptotic convergence rate decays slightly as the computational degrees of freedom increases. Computed velocity magnitude contours on the finest resolution mesh are presented for the $p = 3$ compact scheme in Fig. 10. The mesh is uniformly adapted to the wall using blocks with linear dimension $N = 16$. As with the vortex convection example (Fig. 8), the computed contours do not

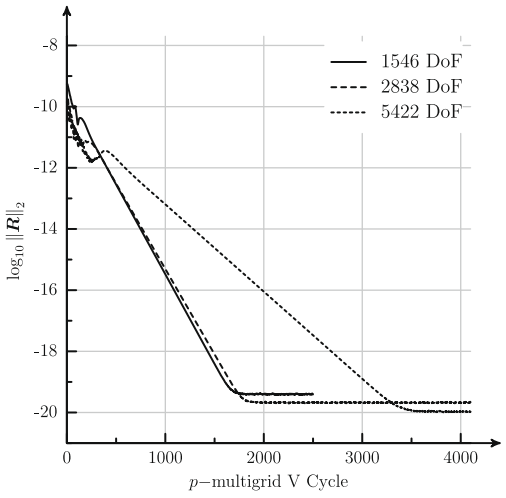


**Fig. 9.** Convergence of the $p$-multigrid scheme with increasing resolution for the compact upwind scheme, $p = 3$, on a laminar flat plate simulation.

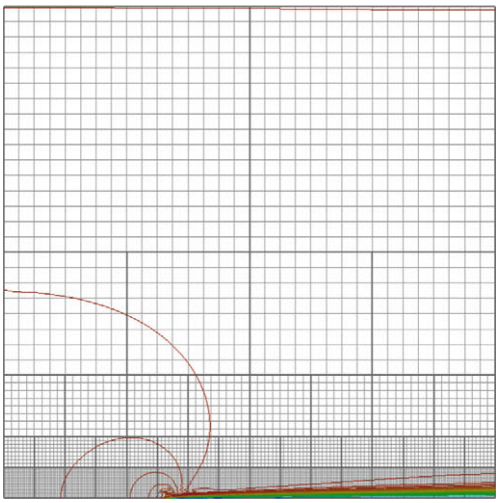

**Fig. 10.** Velocity magnitude profiles for the laminar flat plate boundary layer, $|u| \in [0, |u_\infty|]$. The octree mesh is uniformly adapted to the wall located at the lower boundary. ($M_\infty = 0.2, Re_L = 10^4$).

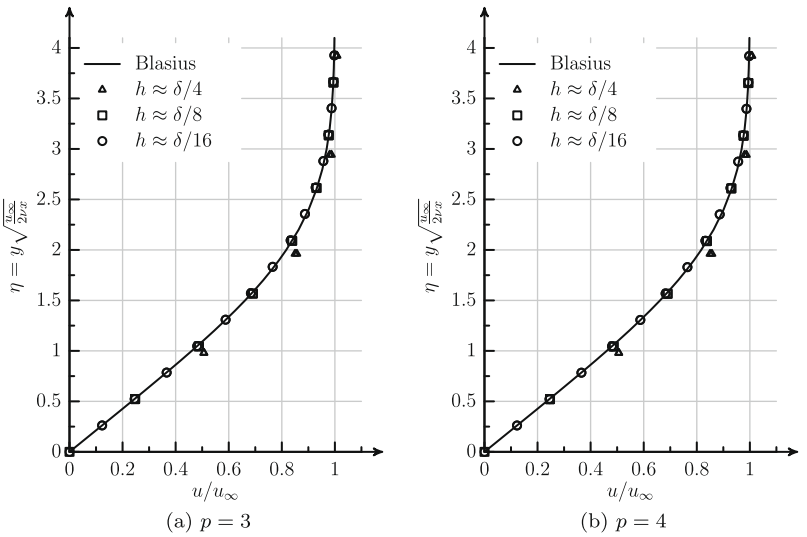


**Fig. 11.** Velocity profiles for the laminar flat plate boundary layer. The disjoint cell interface values are presented. The similarity scaling is determined using a theoretical leading edge for each simulation based upon the computed skin friction.

contain high-frequency oscillations, though the steep gradients at the leading edge are under-resolved. This does not affect the asymptotic (as $x \to L$) behavior of the boundary layer.

Computed velocity profiles with increasing mesh resolution at the outflow edge of the computational domain are presented in Fig. 11 for the compact upwind schemes. Both schemes converge to the theoretical velocity profile without overshoots or requiring additional dissipation.

## 6. Isotropic turbulence

The final computational example simulates three-dimensional homogeneous isotropic turbulence. A cube with edge length $2\pi$ and periodic boundaries forms the computational domain. Spectral forcing based on the approach of Eswaran and Pope [30], with compressible modifications by Paoli and Shariff [31], acts as the energy-producing eddies generating isotropic turbulent fluctuations. In this method low-frequency spectral modes are accelerated using a stochastic forcing until a statistically stationary flow is achieved (cf. Fig. 12). Here, the modes between the spherical shells $6 \leqslant |\boldsymbol{\kappa}| \leqslant 10$ are forced, where $\boldsymbol{\kappa}$ is the vector wavenumber, for a total of 92 forcing modes. The computational domain is isotropically subdivided

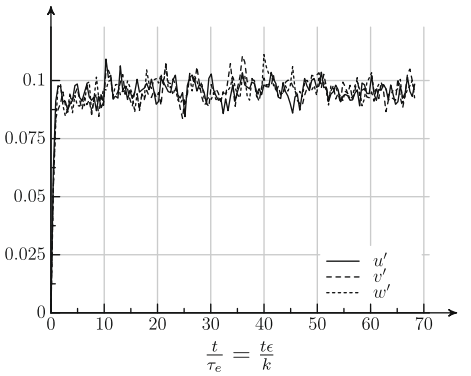


**Fig. 12.** Computed velocity fluctuations for the forced isotropic turbulence. Every 1200th timestep is plotted. Time scaled by the turbulent eddy turnover time. ($p = 3, N = 128^3$).

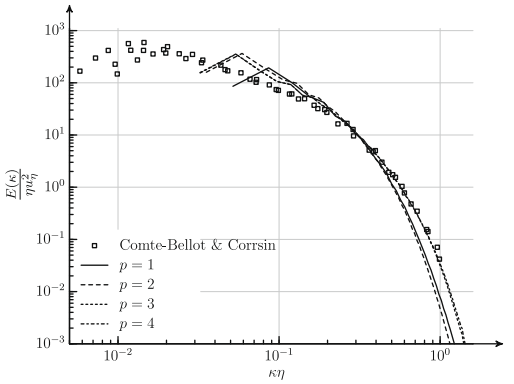


**Fig. 13.** Computed energy spectrum for the forced isotropic turbulence. Experimental data from [32], ($N = 128^3$).

through four levels with a node dimension $N = 16$, for a domain with $128^3$ degrees of freedom in 512 structured blocks. The mesh remains isotropic to facilitate the spectral post-processing. A constant freestream Mach number of $M_\infty = 0.2$ is prescribed, hence we take a statistical "snapshot" of grid-generated turbulence at a single location downstream from the grid. The unit Reynolds number is $Re = 10^2$, and Roe's approximate Riemann solver is again used throughout.

The computed energy spectrum, scaled by the Kolmogorov length scale, for increasing order of the polynomial basis is presented in Fig. 13. The computed results are compared against experimental measurements by Comte-Bellot and Corrsin [32]. The effect of the non-physical spectral forcing is evident in the low wavenumber modes, however the accelerated forcing does provide a convenient method to produce a viscous cascade of energy through the higher wavenumber spectrum. The explicit low-order reconstructions do not accurately represent the higher-frequencies of the turbulent energy spectrum for these computed conditions, as the physical viscosity is augmented by (spurious) numerical dissipation. The implicit higher-order schemes exhibit the beneficial broad spectrum resolution typical of compact schemes, and reconstruct the energy cascade to higher wavenumbers than the traditional explicit methods. As with the previous numerical examples, there is little to distinguish the results of the compact $p = 3$ and $p = 4$ schemes.

## 7. Summary

Novel compact fourth- and fifth-order upwind schemes based on a variable reconstruction finite-volume formulation were derived. Numerical examples using an adaptive-octree mesh demonstrate the formal accuracy of the schemes, the behavior in wall-bounded regions, and the resolution of a broad wavenumber spectrum for the two- and three-dimensional Euler and Navier–Stokes equations. The adaptive octree uses *h*-refinement and timestep sub-cycling to resolve multiple length scales. The combination of practical higher-order upwind methods and localized adaption using structured blocks, provides a building-block towards automated and efficient schemes for applications involving disparate length scales.

## Acknowledgment

Thanks to Dr. Karim Shariff of NASA Ames Research Center for suggesting the spectral forcing method to generate isotropic turbulence.

## References


[1] R. Gomez, D. Vicker, S.E. Rogers, M.J. Aftosmis, W.M. Chan, R. Meakin, S.M. Murman, STS-107 Investigation ascent CFD support, AIAA Paper 2004-2226, 2004.
[2] S.M. Murman, M.J. Aftosmis, S.E. Rogers, Characterization of space shuttle ascent debris aerodynamics using CFD methods, AIAA Paper 2005-1223, 2005.
[3] S.A. Pandya, S.M. Murman, V. Sankaran, Unsteady computations of a jet in crossflow with ground effect, AIAA Paper 2003-3890, 2003.
[4] S.M. Murman, Dynamic simulations of atmospheric-entry capsules, Journal of Spacecraft and Rockets 46 (4) (2009) 829–835.
[5] W.N. Dawes, S.A. Harvey, S. Fellow, C.F. Favaretto, A. Velivelli, Viscous layer meshes from level sets on cartesian meshes, AIAA Paper 2007-555, 2007.
[6] S.L. Karman Jr., Unstructured viscous layer insertion using linear-elastic smoothing, AIAA Journal 45 (1) (2007) 168–180.
[7] J. Sitaraman, A. Katz, B. Jayaraman, A.M. Wissink, V. Sankaran, Evaluation of a multi-solver paradigm for CFD using overset unstructured and structured adaptive cartesian grids, AIAA Paper 2008-660, 2008.
[8] J.E. Flaherty, R.M. Loy, M.S. Shephard, B.K. Szymanski, J.D. Teresco, L.H. Ziantz, Adaptive local refinement with octree load-balancing for the parallel solution of three-dimensional conservation laws, Journal of Parallel and Distributed Computing 47 (1997) 139–152.
[9] E.F. Charlton, K.G. Powell, An octree solution to conservation-laws over arbitrary regions (OSCAR), AIAA Paper 97-0198, 1997.
[10] S.K. Lele, Compact finite difference schemes with spectral-like resolution, Journal of Computational Physics 103 (1992) 16–42.
[11] B. Cockburn, C.-W. Shu, Nonlinearly stable compact schemes for shock calculations, SIAM Journal on Numerical Analysis 31 (3) (1994) 607–627.
[12] D. Fu, Y. Ma, High order accurate difference scheme for complex flow fields, Journal of Computational Physics 134 (1) (1997) 1–15.
[13] K.S. Ravichandran, Higher order KFVS algorithms using compact upwind difference operators, Journal of Computational Physics 130 (1997) 161–173.
[14] X. Zhong, High-order finite-difference schemes for numerical simulation of hypersonic boundary-layer transition, Journal of Computational Physics 144 (1998) 662–709.
[15] N.A. Adams, K. Shariff, A high-resolution hybrid compact-ENO scheme for shock-turbulence interaction problems, Journal of Computational Physics 127 (1996) 27–51.
[16] X. Deng, H. Maekawa, Compact high-order accurate nonlinear schemes, Journal of Computational Physics 130 (1997) 77–91.
[17] J. Ramboer, S. Smirnov, C. Lacor, Finite volume formulation of compact upwind schemes for CAA and LES applications, AIAA Paper 2003-3967, 2003.
[18] D.P. Lockhard, K.S. Brentner, H.L. Atkins, High accuracy algorithms for computational aeroacoustics, AIAA Paper 94-0460, 1994.
[19] D.V. Nance, K. Viswanathan, L.N. Sankar, Low-dispersion finite volume scheme for aeroacoustic applications, AIAA Journal 35 (2) (1997) 255–262.
[20] D.V. Gaitonde, J.S. Shang, Optimized compact-difference-based finite-volume schemes for linear wave phenomena, Journal of Computational Physics 138 (1997) 617–643.
[21] G.-S. Jiang, C.-W. Shu, Efficient implementation of weighted ENO schemes, Journal of Computational Physics 126 (1996) 202–228.
[22] M.H. Carpenter, D. Gottlieb, S. Abarbanel, The stability of numerical boundary treatments for compact high-order finite-difference schemes, Journal of Computational Physics 108 (2) (1993) 272–295.
[23] D.V. Gaitonde, M.R. Visbal, Padé-type higher-order boundary filters for the Navier–Stokes equations, AIAA Journal 38 (11) (2000) 2103–2113.
[24] M.J. Berger, P. Colella, Local adaptive mesh refinement for shock hydrodynamics, Journal of Computational Physics 82 (1989) 64–84.
[25] C.W. Gear, Numerical Initial Value Problems in Ordinary Differential Equations, Prentice Hall, 1971.
[26] H-C. Yee, N.D. Sandham, M.J. Djomerhri, Low-dissipative high-order shock-capturing methods using characteristic-based filters, Journal of Computational Physics 150 (1) (1999) 199–238.
[27] M.-S. Liou, A Sequel to AUSM: AUSM$^+$, Journal of Computational Physics 129 (1996) 364–382.
[28] E.M. Rønquist, A.T. Patera, Spectral element multigrid I. Formulation and numerical results, Journal of Scientific Computing 2 (4) (1987) 389–406.
[29] P.L. Roe, Approximate Riemann solvers, parameter, vectors, and difference schemes, Journal of Computational Physics 43 (1981) 357–372.
[30] V. Eswaran, S.B. Pope, An examination of forcing in direct numerical simulations of turbulence, Computers and Fluids 16 (3) (1988) 257–278.
[31] R. Paoli, K. Shariff, Turbulent condensation of droplets: direct simulation and a stochastic model, Journal of the Atmospheric Sciences 66 (3) (2009) 723–740.
[32] G. Comte-Bellot, S. Corrsin, Simple Eulerian time correlation of full- and narrow-band velocity signals in grid-generated, 'isotropic' turbulence, Journal of Fluid Mechanics 48 (2) (1971) 273–337.